Eur. Phys. J. D (2018) 72: 93
https://doi.org/10.1140/epjd/e2017-80419-8

THE EUROPEAN PHYSICAL JOURNAL D

Regular Article

Plasma based formation and deposition of metal and metal oxide nanoparticles using a gas aggregation source*

Oleksandr Polonskyi[1,a], Amir Mohammad Ahadi[1,b], Tilo Peter[1,c], Kenji Fujioka[2], Jan Willem Abraham[2], Egle Vasiliauskaite[1], Alexander Hinz[1], Thomas Strunskus[1], Sebastian Wolf[2], Michael Bonitz[2], Holger Kersten[3], and Franz Faupel[1]

[1] Chair for Multicomponent Materials, Faculty of Engineering, Christian-Albrechts-Universität zu Kiel, Kaiserstr. 2, 24143 Kiel, Germany
[2] Institute of Theoretical Physics and Astrophysics, Christian-Albrechts-Universität zu Kiel, Leibnizstrasse 15, 24098 Kiel, Germany
[3] Institute of Experimental and Applied Physics, Plasma Technology, Christian-Albrechts-Universität zu Kiel, Leibnizstrasse 11-19, 24098 Kiel, Germany

Received 19 June 2017 / Received in final form 2 October 2017
Published online 25 May 2018 –

Abstract. Metal clusters and nanoparticles (NPs) have been studied intensively due to their unique chemical, physical, electrical, and optical properties, resulting from their dimensions, which provided host of applications in nanoscience and nanotechnology. Formation of new materials by embedding NPs into various matrices (i.e. formation of nanocomposites) further expands the horizon of possible application of such nanomaterials. In the last few decades, the focus was put on the formation of metallic and metal oxide NPs via a so-called gas aggregation nanoparticle source employing magnetron sputtering (i.e. Haberland concept). In this paper, an overview is given of the recent progress in formation and deposition of NPs by the gas aggregation method. Examples range from noble metals (Ag, Au) through reactive metals (Al, Ti) to Si and the respective oxides. Emphasis is placed on the mechanism of nanoparticle growth and the resulting properties. Moreover, kinetic Monte Carlo simulations were developed to explain the growth mechanism and dynamics of nanoparticle formation depending on the experimental conditions. In addition, the role of trace amounts of reactive gases and of pulsed operation of the plasma on the nucleation process is addressed. Finally, the treatment of the NPs in the plasma environment resulting in nanoparticle charging, morphological and chemical modifications is discussed.

1 Introduction

Nanoparticles (NPs) have been the subject of intense investigation in the last few decades due to their unique size-dependent chemical, physical, electrical and optical properties as compared to large micrometer-size particles or bulk material [1,2]. There are many ways of NP generation, from "top-down" approaches, through wet chemical methods, to plasma-based techniques [3]. Here we consider only the latter ones, as they are considered feasible for synthesis of NPs with tunable size distribution, morphology and chemical structure. Close attention was paid in the literature to dusty plasmas, including e.g. hydrocarbon or fluorocarbon plasmas, dealing mainly with larger NPs [4–7]. Moreover, gas aggregation sources (GAS) have recently been utilized to obtain independent control of the size distribution and flux of the metallic NPs, being very efficient, in particular, for synthesis of small NPs [8]. Various metallic and metal oxide NPs were deposited using GAS [9–24]. There are also a number of reports devoted to theoretical approaches to explain the NP formation mechanism in GAS [25–29]. The GAS approach can also be utilized for nanocomposite thin film deposition by embedding NPs into growing polymeric or oxide matrices, permitting easy and independent control of filling factor and size of inclusions [22,30,31].

Despite intensive research over the years, the processes inside the GAS leading to generation of metal and oxide NPs with certain properties are not fully understood yet and still require further investigations.

In the following paper, we report on the recent progress in formation and deposition of NPs by the gas aggregation method. Examples range from noble metals (Ag, Au) through reactive metals (Al, Ti) to Si. Emphasis is placed on the mechanism of nanoparticle formation and their

* Contribution to the Topical Issue "Fundamentals of Complex Plasmas", edited by Jürgen Meichsner, Michael Bonitz, Holger Fehske, Alexander Piel.

[a] e-mail: olpo@tf.uni-kiel.de
[b] *Present address*: Physics Department, Faculty of Science, Shahid Chamran University of Ahvaz, Ahvaz, Iran.
[c] *Present address*: X-FAB MEMS Foundry Itzehoe GmbH, Fraunhoferstrasse 1, 25524 Itzehoe, Germany.

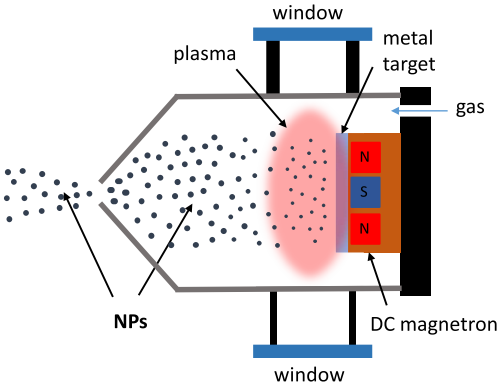

Fig. 1. Schematic drawing of the gas aggregation nanoparticle source.

properties. Moreover, kinetic Monte Carlo (KMC) simulations were developed to explain the growth mechanism and dynamics of cluster formation depending on experimental parameters. Moreover, the role of trace amounts of reactive gases and of pulsed operation of magnetron sputtering on the nucleation and growth process is addressed. Finally, the "in-flight" plasma treatment of the NPs resulting in nanoparticle charging, morphological and chemical modifications is discussed.

This paper is organized as follows. First, in Section 2, the details of a GAS source are given. Section 3 is devoted to KMC simulations of the growth of NPs in a GAS. Sections 4 and 5 are focused on the experimental finding with noble and reactive NPs, respectively. Finally, "in-flight" plasma treatment of Ag NPs is discussed in Section 6, followed by a summary.

2 Gas aggregation nanoparticle source

The very original design of a GAS involved thermal evaporation, which served as a source of atomic metal vapors, following subsequent condensation induced by a buffer gas (typically Ar) [10,17,32]. Later, Haberland suggested replacing the thermal evaporator by magnetron sputtering to generate ionized metallic NPs [12]. A typical GAS (also commercially available) consists of a tubular chamber equipped with a direct current (DC) planar magnetron which serves as a source of material (Fig. 1).

Usually, magnetron sputtering in a GAS is done at a relatively high gas pressure (up to ∼200 Pa) needed for efficient cluster formation. The process of NP formation in a gas aggregation volume has several steps. First, atoms are sputtered, thermalized by argon or an other inert working gas, and dimer formation starts as a result of three body collisions. In the second step, clusters grow by atom attachment. When the clusters are big enough, coagulation can contribute to NP growth [26]. Following a co-axial gas flow towards the conical shape at the end of the GAS, NPs are transported from the plasma zone through a small orifice into the low pressure (typically 0.5–2 Pa) deposition chamber. Here, the beam of NPs is focused with almost no interactions among them. The divergence of the beam is typically small (∼5°–10°) and depends on both pressures in the GAS and in the deposition chamber, as well as on the gas flow and dimensions of the orifice [33,34]. In the deposition chamber, the GAS-synthesized NPs can be collected on solid supports or embedded into a host matrix using a co-deposition technique and, thus, form nanocomposite thin films.

To tailor NP generation and deposition, the following physical parameters of the GAS can be modified: dimensions of the magnetron, aggregation length, orifice diameter, shape, and length. Experimental parameters to be varied are typically the following: magnetron power, gas pressure/flow, target material and reactive gas admixtures.

3 Kinetic Monte Carlo simulations of the growth nano-sized clusters in a GAS

The cluster growth in a GAS takes place on length and time scales which are far out of scope of typical ab initio simulation methods. As has been discussed in a paper by Abraham et al. in the same issue of this journal [35], the most accurate simulations of nanocluster growth are usually provided by atomistic molecular dynamics (MD) in cases where elaborate MD acceleration techniques can be applied [36]. However, we currently assume that only statistical methods can handle the very complex dynamics and large system sizes involved in the formation of metal clusters in a GAS. Therefore, we developed a KMC simulation model that is capable of expressing the evolution of metal cluster growth in terms of fundamental processes and corresponding rate constants [37]. Instead of calculating complete trajectories of the particles, only transitions between pre-defined system states are considered in KMC. If all relevant processes p_i are Markovian, the waiting times τ between subsequent occurrences of p_i can be sampled from the exponential distribution

$$f(\lambda_i, \tau) = \lambda_i \exp(-\lambda_i \tau), \quad (1)$$

where λ_i is the rate constant.

In the following, we give a brief explanation of the implemented simulation model. For a complete description including all missing details and a proposition of a KMC algorithm to account for time-dependent process rates, we refer to reference [37]. A more general overview of KMC is given in reference [38]. In Section 3.2, we discuss the simulated size distributions of emitted clusters as a function of selected model parameters and compare then with experimental results.

3.1 KMC simulation model

Making use of the radial symmetry of the aggregation chamber, one central idea of the model is to perform the simulations in a one-dimensional space, which effectively represents the actual three-dimensional physical system. The space is divided into slices with equal lengths and radii (see Fig. 2 for illustration of the slicing and the modeled processes) and is representative of a simple cylindrical geometry for the aggregation chamber. In principle, more complex geometries may be modeled by varying the

dimensions of slices in the space. Each slice is assigned a locally uniform density n_α for each particle species α. The buffer gas is assumed to merely provide background conditions which enter in the rate constants of the modeled cluster processes. It has a constant density, n_g, that remains unaffected during the course of a simulation. The sputtered free metal atoms are not modeled explicitly either. Instead, a balance between the source (sputtering) and drain (diffusion to walls, cluster formation) of free atoms is assumed leading to a static density profile $n_\mathrm{m}(z)$.

3.1.1 Description of clusters

As has been shown in previous KMC studies of metal cluster growth, an appropriate way to reduce the computational effort is to dispense with an atomistic description and employ a continuous description of clusters instead [39–42]. We follow this approach and treat all clusters as perfect spheres with a uniform density of atoms. According to the liquid-drop model, a cluster containing N atoms with the Wigner–Seitz radius r_WS is assigned the volume

$$V = N\frac{4\pi}{3}r_\mathrm{WS}^3. \tag{2}$$

3.1.2 Nucleation

The nucleation of clusters is modeled by inserting dimers into the simulation box. As a time-independent monomer-density is assumed, dimers are the smallest clusters that are explicitly modeled. This process is considered to be memoryless. Its waiting times are sampled from an exponential distribution, equation (1), with the rate

$$\lambda_\mathrm{N} = Kn_\mathrm{m}^2 n_\mathrm{g} V, \tag{3}$$

where K is a three-body collision constant and V is the volume that is associated with a slice.

3.1.3 Transport

The motion of clusters is represented by subsequent hopping events between adjacent slices, according to the lattice Monte Carlo method presented in reference [43]. For that purpose, each cluster is assigned a size-dependent time $\langle t\rangle$ to attempt a transition to another slice. A random process is used to decide whether the cluster moves forwards, backwards, or stays at its current position, with the buffer gas drift velocity imparting a bias to move forward towards the chamber's orifice. Another transport process has been implemented to account for clusters which move diffusively and stick to the chamber walls. This is a size-dependent process which occurs more often for small clusters. Each cluster that reaches the chamber wall is excluded from further simulation.

3.1.4 Growth

Two processes have been implemented to model the growth of the clusters. All growth events lead to instantaneous updates of the cluster volumes according to equation (2). The first process describes the attachment of a free metal atom to a cluster when they collide. Due to the strong metallic bonds, it is assumed that the sticking probability is always one. The waiting times of the collisions can be sampled from an exponential distribution. However, instead of incrementing the cluster sizes by the addition of single atoms, larger jumps between cluster sizes are simulated via the introduction of a size index, where the number of atoms in a cluster is proportional to the index raised to a power, $N_i \propto i^p$. The waiting times for the summarized atom attachment events are sampled from an Erlang distribution [37]. Since fewer simulation steps are needed to achieve large clusters the simulation time for growth can be significantly reduced while maintaining nearly full accuracy. For example, a cluster of 10^6 atoms may be simulated in 10^3 steps with $p = 2$. In practice however, the movement of clusters through the simulation represents a bottleneck that reduces the improved computation time to a net factor of 10.

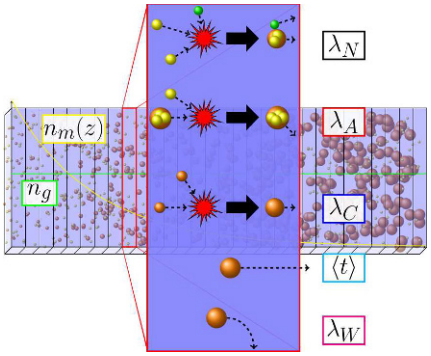

Fig. 2. Schematic of the 1D cluster growth model used in our KMC simulations. The curves indicate the background densities of gas atoms (n_g) and free metal atoms [$n_\mathrm{m}(z)$]. The enlarged slice highlights the included processes and rates (from top): cluster nucleation, atom attachment, coagulation, movement, and wall diffusion.

The other process represents the coalescence of two clusters after a collision. The corresponding rate for a collision of a cluster with size N and another cluster of size M is given by

$$\lambda_{NM} = n_M \kappa_{NM}, \tag{4}$$

where n_M is the number density of clusters with size M, and κ_{NM} is a coagulation kernel. Estimating that the ratio of the mean free path of clusters with respect to the buffer gas and the mean distance between two clusters is less than one, κ_{NM} can be expressed by a diffusion kernel according to references [44,45]. As it is unlikely that a collision of two clusters always leads to coalescence, the algorithm contains a limitation of the sticking efficiency. This is realized by claiming that coalescence only takes place after a collision event if the radii of the colliding clusters are below the value R which is sampled from the log-normal distribution

$$f(R;\mu,\sigma) = \frac{1}{R\sigma\sqrt{2\pi}}\exp\left[-\frac{(\ln(R)-\mu)^2}{2\sigma^2}\right] \tag{5}$$

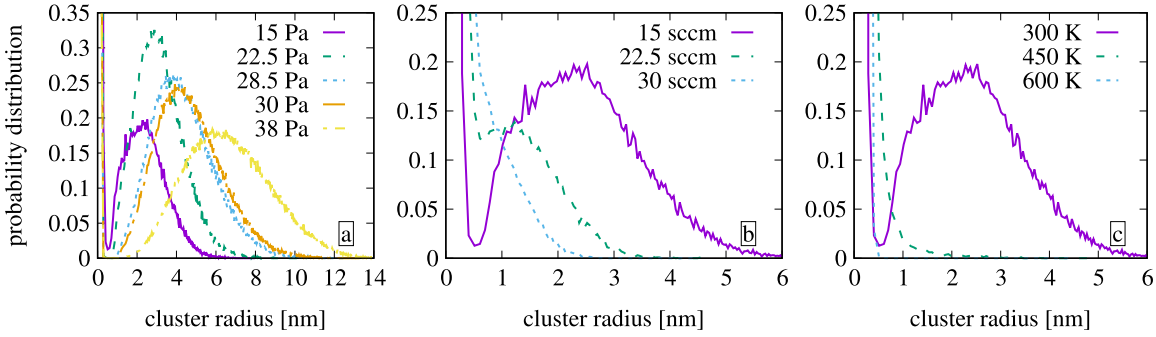

Fig. 3. Influence of buffer gas pressure (a), flow rate (b) and temperature (c) on cluster size distributions as predicted by KMC simulations [37]. Unless the figures indicate a variation of the parameters, the corresponding simulations have been carried out at temperature 300 K, the buffer gas pressure 19 Pa and the Ar flow rate 15 sccm.

with $\mu = \ln(r_c/\sqrt{1+\sigma_c^2/r_c^2})$ and $\sigma^2 = \sqrt{\ln(1+\sigma_c^2/r_c^2)}$. The mean r_c and the variance σ_c^2 must be fitted to match experimental conditions. Typically, the values of r_c are on the order of the critical cluster radius for which a cluster undergoes a phase transition from liquid to solid.

3.2 KMC simulation results

In reference [37], comprehensive parameter studies have been performed to test the KMC model and compare with experimental results. Here, we concentrate on the simulated size distribution of emitted clusters. The model parameters were chosen such that they correspond to Cu cluster growth in an Ar buffer gas with experimental conditions similar to those presented in references [46,47]. If we do not explicitly mention variations of the parameters, all of the presented results have been obtained for the magnetron chamber length 12 cm, the temperature $T = 300$ K, the buffer gas pressure 19 Pa and the Ar flow rate 15 sccm.

3.2.1 Buffer gas properties

In Figure 3 we show how the buffer gas properties affect the size distribution. As clusters with less than 100 atoms usually cannot be detected in experiments, we will not discuss the peaks that occur for very small cluster radii below 0.5 nm.

In Figure 3a, we find that an increase of the gas pressure shifts the mean cluster size to larger values. This primarily happens because of the following two reasons: first, an increase of the pressure slows down the diffusion and drift velocity of the clusters. Hence, the residence time of the clusters in the chamber is extended, which allows for more growth events to take place. Second, the increased pressure also creates higher densities of free metal atoms, which leads to higher nucleation and atom attachment rates.

In Figure 3b, we demonstrate the influence of the buffer gas flow rate. An increase of the flow rate results in larger drift velocities and lower densities of free metal atoms. The effects are, hence, opposite to the effects of increasing the pressure. As the data show, the occurrence of a local peak cluster radius can be completely suppressed by doubling the flow rate from 15 sccm to 30 sccm.

In Figure 3c, we show that doubling the temperature from 300 K to 600 K has a similar, but even stronger effect. As the ideal gas law applies to the buffer gas, an increase of pressure (holding temperature constant) drives up the buffer gas density, effecting the processes mentioned above with respect to Figure 3a. Conversely, increasing the temperature with a fixed pressure means a decrease in the buffer gas density and hence we expect the opposite effect as that of increasing pressure (Fig. 3a). But temperature also enters in other process rates that do not explicitly depend on the buffer gas pressure as well. An increase in the temperature leads to reduced movement times, nucleation rates, atom attachment rates, and coagulation rates. The effect on the nucleation rate is particularly strong as it scales with T^{-3}.

3.2.2 Critical radius

Finally, in Figure 4, we show a set of results for different values of the critical radius r_c and make a comparison with experimental data from reference [46]. The melting point depression of small clusters serves as the physical motivation for a critical radius. Heuristically, we would not expect two solid macroscopic clusters to coalesce upon collision. We could, however, expect coalescence to be aided if the clusters' volumes or surfaces are molten upon collision. The melting point depression model presented in reference [48] permits clusters with radii $\leq$0.6 nm to be fully molten and thus are ideal candidates for coalescence. With r_c we allow for larger clusters to coalesce as well. These clusters are thought to have surfaces which are already in a liquid state or which may gain enough energy in a collision event to locally liquify, thus allowing coalescence.

According to equation (5), an increase of r_c makes it more likely that large clusters undergo coagulation. Therefore, an increase of r_c shifts the peak in the size distribution to larger radii. At the same time, it becomes noticeable for $r_c = 1.5$ nm and $r_c = 2$ nm that this also leads to a minimum in the size distribution, due to a depletion of clusters with intermediate sizes.

The best agreement with the experimental data is achieved for $r_c = 2$ nm. Both the width of the peak displaying the most probable cluster size and its position are reflected by the simulation results. However, the

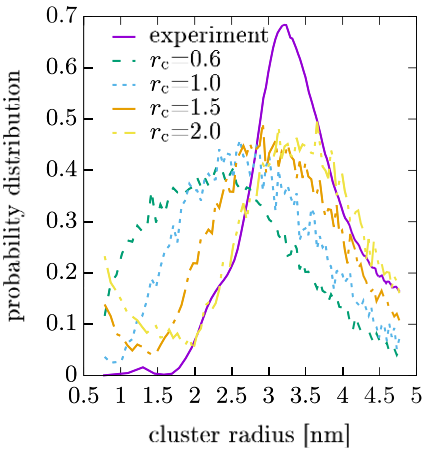

Fig. 4. Dependence of the cluster size distribution on the critical cluster radius r_c (see Eq. (5)) in KMC simulations and comparison with experimental data from reference [46].

simulations predict too large probabilities for clusters with radii below 2 nm and the second peak of the experimental curve between 1 nm and 1.5 nm cannot be reproduced either. The reasons for these deviations remain to be found in future investigations.

3.3 Concluding remarks on the simulations

For the choice of a specific computational method, one always has to make a compromise between accuracy and computation time. KMC is based on a strongly coarse-grained description, but it allows for comprehensive qualitative explorations of macroscopic phenomena. Although the present model requires the introduction of free parameters such as the critical radius, the relatively short computation times allow one to find appropriate values with the help of extensive parameter scans. Another advantage of KMC is that it allows for systematic improvements by implementing new processes or refining the rate constants. As we showed above, the simulation model in its current state already confirms experimental observations to a large extent. Nevertheless, we expect that better agreement can be achieved in the future by implementing a mechanism for partial coalescence of clusters and by finding more accurate expressions for the sticking efficiency of clusters.

4 Deposition of noble metal (Au, Ag) NPs and their nanocomposite thin films using a GAS

An example of Ag NPs produced by GAS is demonstrated in Figure 5 where a TEM image of sub-monolayer coverage of NPs is shown together with the corresponding size distribution [49]. To obtain low coverage and prevent agglomeration of NPs on the substrate the deposition time needs to be short (∼1 s in this case). Most GAS-deposited NPs are nearly spherical in shape since they do not grow in a diffusion-limited aggregation regime. Exceptions are NPs formed via agglomerations due to cluster–cluster collisions in flight or on the substrate, if NP coverage is at least one monolayer. Due to depression of the melting point, clusters are in a liquid state in the GAS close to the target surface. Bigger clusters are solidified, but thermal energy, due to atom attachment and cluster–cluster collision, is still sufficient to allow relaxation to a spherical shape. However, complete re-crystallization is not always possible and resultant NPs stay in a poly-crystalline form, containing 2–4 nm sized domains corresponding well to the expected solidification at room temperature.

Longer deposition times lead to the formation of agglomerated porous films (Fig. 6). Such films are grown by agglomeration of individual NPs that form linked networks with metallic bonds. Due to their high porosity, such films, absorb light and, thus are black in color. GAS deposition on solid supports results in a dark "spot" with a round shape. The thickness of such a deposit has a maximum in the center and gradually decreases toward the edge. In our case, the profile of the deposit follows a Lorenz shape with varying full width at half maximum (FWHM) depending on the GAS pressure and orifice-substrate distance (Fig. 6c). However, the size and shape of the deposited "spot" strongly depends on the experimental parameters and the geometry of the GAS nozzle [50]. NPs from a GAS are deposited in a soft landing regime and have very low adhesion to the substrate surface [51]. To improve surface adhesion, one can use electrostatic acceleration of charged NPs or embed them into the matrix [20,31,52].

Generally, the size of NPs produced by a GAS can be varied in the range up to ∼100 nm. The main parameters influencing NP size are magnetron power (density of sputtered atoms), gas flow (residence time in a GAS volume) and aggregation pressure (mean free path, number of collisions). Figure 7 shows SEM images of Ag NPs having different sizes. They were deposited using the same GAS system operating at different Ar flow rates and pressures, which dramatically influence the size of NPs. As one can see, nearly monodispersed NPs were generated (Figs. 7a, 7b) and the size of NPs can be varied in a broad range by proper tuning of Ar flow and/or aggregation pressure (Fig. 7c) as also predicted by computer simulations (see Sect. 3). However, one should take into account that in Figure 7c the aggregation pressure was varied by varying a gas flow; thus, the influence of both parameters (i.e. pressure and flow) on NP growth is important. According to KMC simulations, gas flow and pressure have opposite effects on the size of NPs (e.g. high flow rate leads to small NP generation). Therefore, Figure 7c demonstrates that Ar flow has a stronger effect on NP size than the resulting aggregation pressure. So, GAS is a very attractive tool for generation of NPs with a desired size distribution and properties. Even without size filtering, e.g. with a quadrupole mass filter [53,54], which drastically reduces the deposition rate, narrow size distributions can be obtained together with high deposition rates.

Although the examples discussed above were based on Ag NP formation and deposition, a GAS has similar performance with other noble metals (e.g. Au, Cu or Pt) [24,55–58]. Nevertheless, a certain "window" of

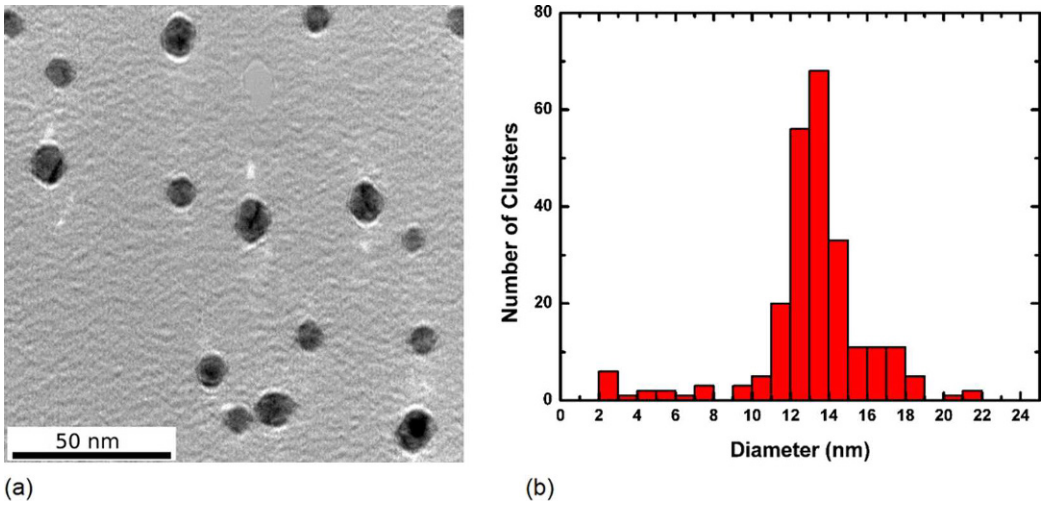

Fig. 5. Deposited Ag clusters: (a) TEM image of single clusters from a very short deposition time (1 s) at 50 W and 200 Pa, (b) histogram with corresponding size distribution by numbers of clusters (adapted with permission from [49]).

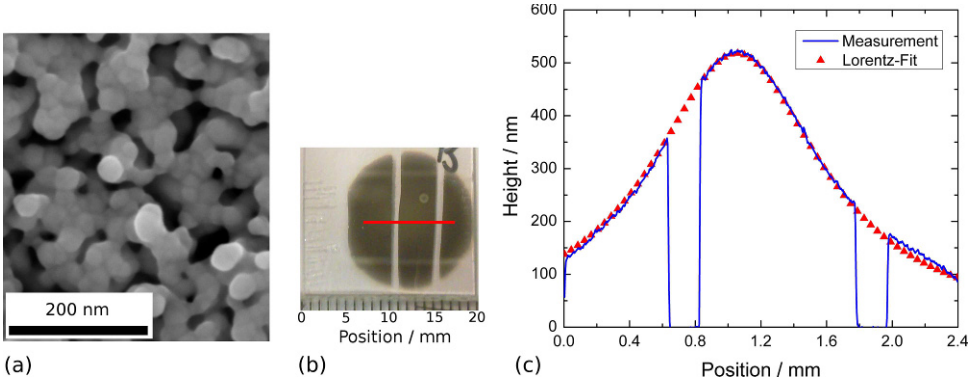

Fig. 6. SEM image of a porous film of NPs deposited at 30 W and 160 Pa for a time of 120 s (a), photograph of a typical deposited sample onto a glass substrate (b), contact profilometer measurement with fit at the red line shown in (b) (reprinted with permission from [49]).

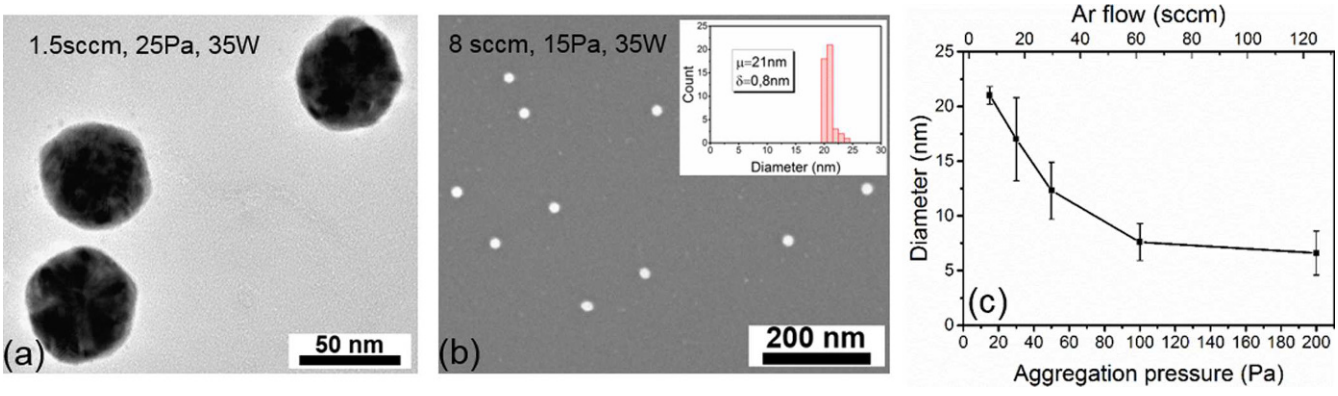

Fig. 7. Size dependence of Ag NPs on experimental parameters: (a) large Ag NPs; (b) small Ag NPs; (c) NP diameter vs. Ar flow/pressure in a GAS (vertical bars indicate FWHM of size distributions).

parameters (i.e. magnetron power, gas flow and pressure), needs to be experimentally determined in order to get the desired size or size distribution of the respective NPs. In this case, the results of computer simulations (discussed above) become particularly useful, giving hints on how the parameters should be selected for desired NP properties. The reason for differences in the required experimental conditions for different metals relates to material specific properties (e.g. melting point, sputtering yield, etc.) which influence cluster nucleation and growth [26]. An example of GAS-deposited Au NPs given in Figure 8 shows a UV–vis spectrum together with SEM topography. Here, Au NPs with a mean diameter of around 35 nm show localized surface plasmon resonance (LSPR) at around 525 nm, which is in a good agreement with results reported in the literature [59].

A combination of a GAS NP beam and a growing polymer or ceramic matrix (e.g. metal oxide reactively or radio frequency (RF) sputtered) provides an opportunity for nanocomposite thin film formation. The advantage of independent NP size variation and control over the deposition rate of the matrix allows one to create nanocomposites with different filling factors and variable inclusions, and therefore different properties [22,49,60–62]. However, a few issues related to synthesis of nanocomposites using co-deposition have to be mentioned here. First, if the secondary source (source of a matrix) utilizes a plasma discharge, like magnetron or RF plasma source, deflection of the NP beam by electrostatic forces may occur, since most of GAS generated NPs are charged [63]. In order to overcome this problem, pulsing the matrix deposition can be considered [22,31]. Second, nanocomposite thin films formed via co-deposition in combination with a GAS typically have high surface roughness. The reason for this is a strong size discrepancy of the single components of deposited nanocomposite film (e.g. if GAS deposition is combined with magnetron deposition, the size of a single NP is much larger than the size of one atom) [64].

5 Reactive processes in a GAS and their influence on generation of Ti-, Al- and Si-based NPs

Although a GAS is a very efficient tool for NP synthesis with tunable size distribution, reproducibility of NP deposition is very often somewhat problematic. Mainly, irreproducible behavior of GAS was observed for reactive materials, like Al, Co or Ti. Very little attention has been devoted to this aspect in the literature and only a few reports addressed the stability of NP generation by GAS [18,47,65]. We found that for Al and Ti NPs the deposition rate is usually highly unstable and very often it completely vanishes after longer operation of the GAS. Nevertheless, restarting the cluster formation was possible by venting the vacuum system, causing oxidation of the target surface. Detailed investigation of this problem brought us to the conclusion that generation of Ti NPs can be initiated and controlled by admixing a very small amount of oxygen [66]. Figure 9 shows the influence of an oxygen admixture on the deposition rate of Ti NPs. Oxygen gas is needed to

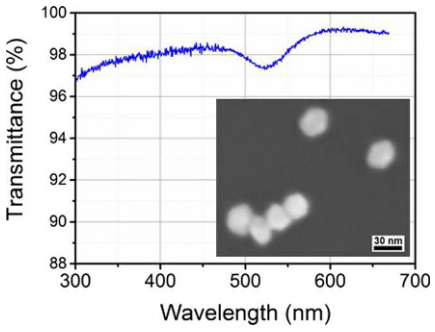

Fig. 8. Transmittance UV–vis spectrum of Au NPs deposited onto quartz substrate. Inset shows SEM image of GAS deposited Au NPs. Deposition parameters: DC power 100 W, Ar pressure 200 Pa, Ar flow 100 sccm. UV–vis measurement was done in the vacuum.

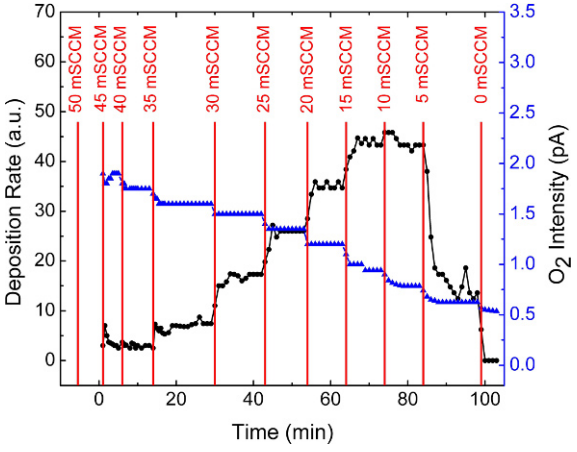

Fig. 9. Influence of reactive gas (oxygen) admixture on Ti NP deposition. Ar pressure is 150 Pa, Ar flow 80 sccm (reprinted with permission from [66]).

stabilize (chemically) small cluster seeds by formation of TiO_x compounds and thus sustain NP growth. However, the amount of admixed reactive gas must be very small to prevent target poisoning and a consequent decrease in sputter rate and efficiency of NP growth. For the chosen experimental conditions (i.e. Ar pressure, magnetron power) there is an optimal amount of oxygen that is needed for the highest deposition rate. A very small deviation in oxygen flow can significantly influence the rate and stability of NP generation, as shown in Figure 10 [67]. The problem of stability of NP generation relates to the complicated reactive processes occurring in a GAS volume during reactive sputtering. Those involve target oxidation, oxygen consumption by growing NPs, oxygen gettering by the Ti coated inner walls of the GAS, etc. [68]. All these factors may spontaneously change the balance between the amount of reactive gas and the density of sputtered atoms, leading to a drop in NP deposition rate.

In order to get better stability and reproducibility of Ti NP deposition, pulsed DC (pDC) magnetron sputtering can be utilized. pDC operation provides better control over the hysteresis of reactive sputtering and, hence, stability of NP synthesis (see Ref. [69] for more details). It

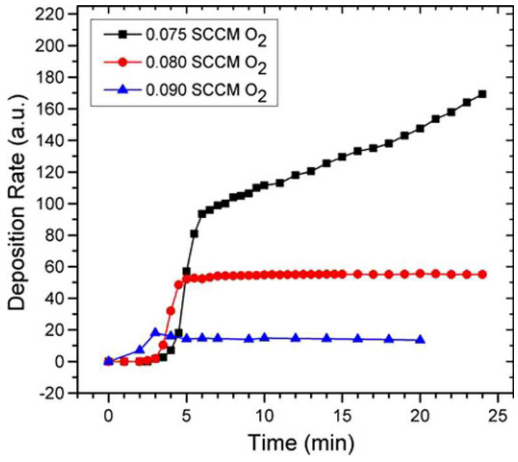

Fig. 10. Time evolution of Ti NP deposition rate with different oxygen admixtures (reprinted with permission from [67]).

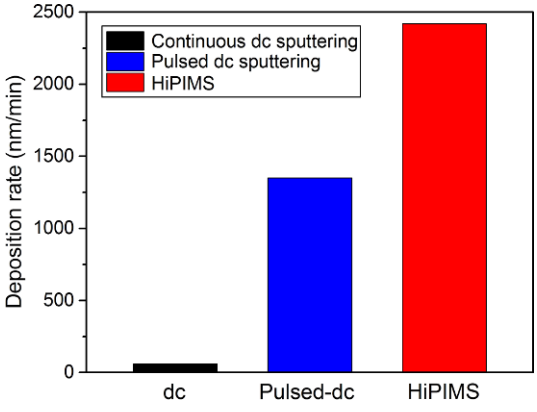

Fig. 11. Huge increase in deposition rate of Ti-based NPs using pulsed magnetron sputtering and HiPIMS. Optimum oxygen concentration was always admixed.

was also found that pDC magnetron operation, in combination with reactive gas admixtures, provides a huge increase in the generation of Ti-based NPs compared to continuous DC (cDC) mode (Fig. 11) [70]. Such enhancement is due to a large amount of Ti oxide compounds formed on the target surface during "time-off" and subsequently sputtered at the power pulse at "time-on" when applying pDC operation, the idea is to keep an equilibrium between target surface oxidation and subsequent sputtering of an oxide layer in the form of TiO_x compounds which serve as building material for NPs [70]. Utilization of high power impulse magnetron sputtering (HiPIMS) provides an even more enhanced deposition rate of Ti-based NPs, reaching around 2.4 μm/min (more than 40 times higher than cDC mode) (Fig. 11).

Obviously, one cannot expect pure metallic Ti NPs if oxygen is involved in the growth process. However, XPS characterization of TiO_x NPs deposited by cDC and pDC modes shows that NPs contain around 50% and 20% of elemental Ti, respectively [69,70].

At some point, using HiPIMS, we were able to synthesize Ti NPs without any oxygen admixture [71]. However, the "window" of parameters permitting such deposition

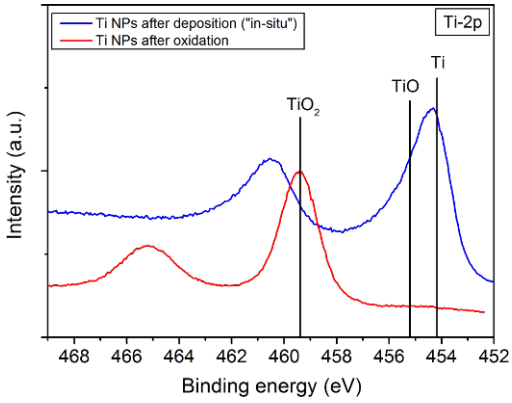

Fig. 12. XPS measurements of Ti NPs deposited using HiPIMS magnetron operation. No oxygen was added during sputtering. Measurements were done in situ just after deposition and ex situ after oxidation in the air.

was relatively narrow and the overall deposition rate was relatively low, being comparable to continuous magnetron operation. Detailed XPS investigation of such Ti NPs, transferred under vacuum conditions to XPS, showed, however, the presence of a small amount of Ti oxides, which could be due to impurities in Ar gas used for sputtering (Fig. 12). Exposure of NPs to the air leads, typically, to their complete oxidation and formation of TiO_2.

The observed stability and enhancement of Ti NP generation by admixed reactive gas can be attributed to diatomic binding energies. In the case of Ti–Ti, the binding energy is 1.2 eV, while for Ti–O dimers it is 6.9 eV, which ensures the survival of Ti–O compounds in the plasma environment of a GAS that serve as cluster seeds [66].

Figure 13 shows an example of Al NPs deposited using a GAS. Here, in analogy with the behavior discussed above for Ti, extra oxygen admixture was required to launch Al NP growth. However, keeping oxygen flow at the lowest possible level necessary for the stability of cluster seeds, we were able to deposit highly metallic NPs showing intense LSPR localized in the UV range (below 300 nm). The inset SEM image (Fig. 13) shows nearly monodisperse, highly crystalline Al NPs with an average diameter of 80 nm. By tuning experimental parameters, the size of the NPs can be easily varied and leads also to a shift of the plasmon resonance peak position [62]. The LSPR of Al NP and its tuning can be used for applications in plasmon-enhanced UV photocatalysis [72].

Deposition of Si/SiO_x NPs was realized using a GAS with magnetron sputtering from a Si target and additional oxygen admixture needed to promote NP growth [73]. To enhance the deposition rate of Si-based NPs, pDC sputtering was utilized. Figure 14 shows a comparison of deposition rates for cDC and pDC magnetron operation as a function of the oxygen admixture flow rate. As one can see, pDC provides much higher efficiency of SiO_x NP generation due to sputtering for SiO_x compounds directly from the target surface (same as for Ti, discussed above). Moreover, cDC magnetron operation shows stronger hysteresis of the deposition rate of NPs.

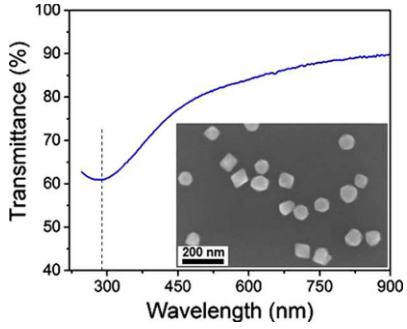

Fig. 13. Transmittance UV–vis spectrum of Al NPs deposited onto quartz substrate. Inset shows SEM image of GAS deposited Al NPs with average diameter 80 nm. Deposition parameters: cDC power 100 W, Ar pressure 30 Pa, Ar flow 5 sccm.

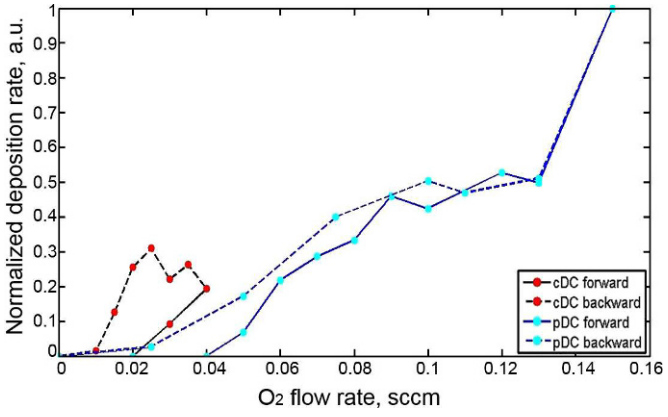

Fig. 14. Comparison of O_2 flow rate influence on SiO_x NP deposition in cDC and pDC operation. Ar = 115 sccm (200 Pa), $P = 50$ W.

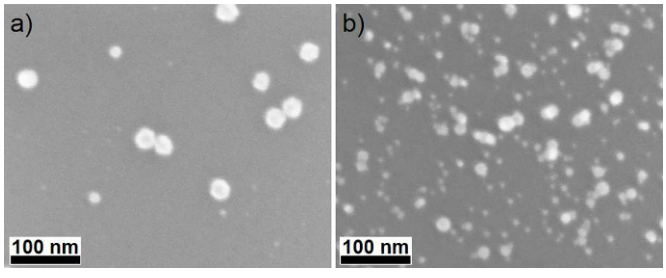

Fig. 15. SEM images of SiO_x NPs deposited by a pDC GAS with different oxygen flow rates: (a) 0.05 sccm, (b) 0.1 sccm. Power 50 W, discharge frequency 40 kHz, duty cycle 50%, Ar 115 sccm (200 Pa).

SEM images of SiO_x NPs deposited at different O_2 admixtures are shown in Figure 15. As one can see, higher oxygen admixture results in more numerous and smaller NPs compared to NPs obtained when using lower admixture. The reason for that can be explained as follows. O_2 flow rate (or amount of O_2) determines how many stable nuclei for NP growth can form (same idea as for Ti or Al). When the O_2 flow rate is higher, there should be more stable nuclei forming and, thus, the growth of the NP will be limited by the amount of sputtered material available per growing nucleus. As a result, small NPs of relatively narrow size distribution will be formed. On the other hand, when the O_2 flow rate is lower, fewer nuclei form and, thus, the growth of clusters is not limited by the amount of material available for growth. Thus one expects that NPs will be less numerous, relatively large, and of a relatively wide size distribution.

A similar effect on NP size distribution was observed also for the applied magnetron power (namely, higher power led to generation of smaller NPs) because of the misbalance between available nuclei and the amount of sputtered material.

The influence of O_2 admixture on Si-based NP chemical composition was investigated by means of XPS. Quantitative analysis of the surface composition of a NP film revealed that in the case of 0.05 sccm oxygen flow, the fraction of elemental Si was around 19.5%, while 0.1 sccm of O_2 flow led to higher oxidation of NPs with elemental Si of only ∼4.5%. However, XPS is a surface sensitive technique and yields information about the topmost layers of the sample, and, since measurements were made ex situ, the oxidation of NPs could have taken place outside the deposition chamber. Therefore, the investigated NPs might have obtained a core-shell structure with a greater amount of elemental Si in the core and with an oxide shell. In any case, the more pronounced Si peak at lower O_2 admixture suggests that the chemical composition can be controlled by the extent of O_2 admixture.

6 "In-flight" plasma treatment of Ag NPs

Fabrication of advanced nanomaterials with desired properties is always of high interest. One approach to get such materials is plasma treatment or the modification of existing ones. We investigated plasma treatment of Ag NPs in an RF hollow cathode (HC) plasma, as shown in Figure 16. Here, Ag NPs synthesized by a GAS (same as shown in Sect. 4) passed through an RF plasma discharge, thus being treated "in-flight". More experimental details can be found in [74,75]. Very interesting results of NP interaction with Ar plasma were obtained, especially concerning NP charging and surface treatment. We found that at low RF power, most of the NPs passing through an RF argon plasma are negatively charged, and only a very small fraction are positively charged or neutral. However, increasing RF power leads to an increase in the fraction of positively charged NPs due to a higher total energy flux to the NP surface and, as a result, a higher probability for the thermoemission of electrons [75].

The charging of Ag NPs in the plasma region influences their deposition. It was shown that a NP beam is disturbed due to electrostatic forces and, as a result, the deposition profile can be varied by varying the RF power (e.g. the beam of NPs can be deflected completely or well-focused onto the substrate) [75].

A Langmuir probe was utilized to characterize the influence of the NPs on the RF discharge. Figure 17 illustrates that with increasing magnetron power, i.e. with increasing number of NPs in the plasma (see above), the electron density decreases while the electron temperature increases

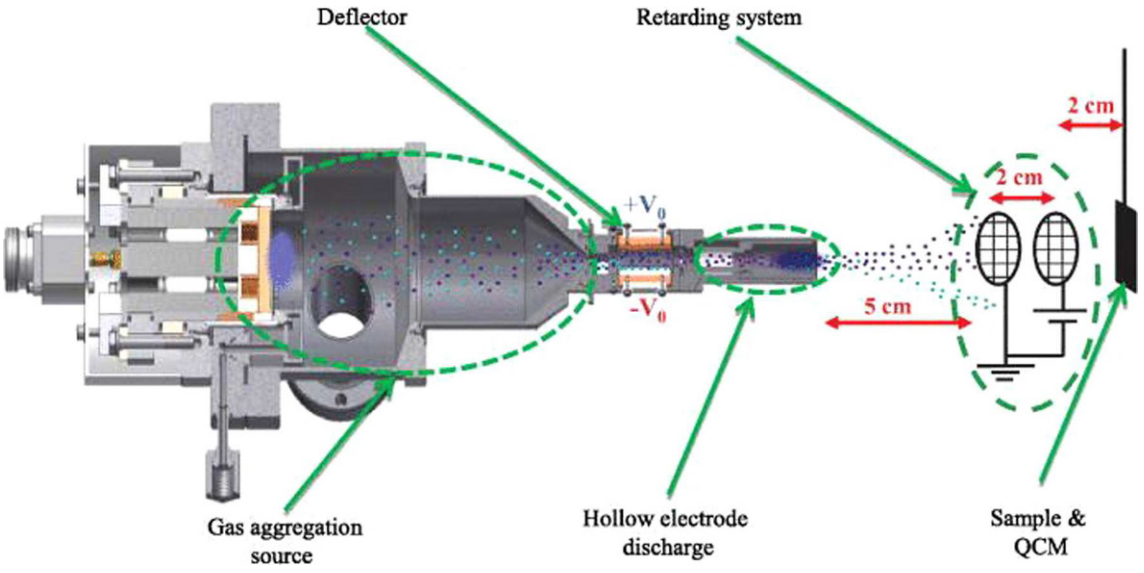

Fig. 16. Scheme of the experimental setup used for "in-flight" NP treatment by an RF hollow cathode. A retarding system was installed for the characterization of the charge distribution of NPs (reprinted with permission from [75]).

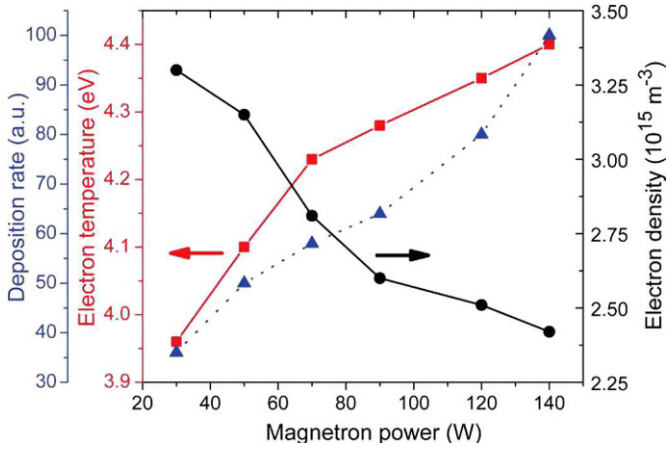

Fig. 17. Plasma parameters obtained by Langmuir probe measurements in the presence of different concentrations of Ag NPs. The dotted blue line indicates the deposition rate. The power of the RF discharge was fixed at 7 W (reprinted with permission from [75]).

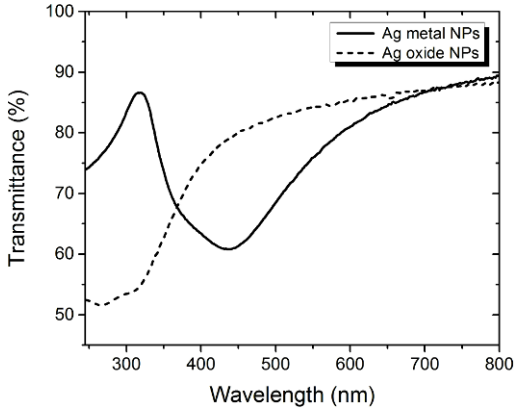

Fig. 18. Transmittance UV–vis spectra of Ag clusters that passed through a hollow cathode discharge with Ar plasma (solid) and oxygen (O_2 to Ar ration is 1:15) plasma (dashed). The blue shift in the plasmon resonance is due to NP oxidation.

slightly. The drop of the plasma density with an increasing number of NPs is explained in terms of electron capturing by NPs, which are further transferred out of the discharge zone.

Similar experiments on "in-flight" plasma treatment of Ag NPs showed that the chemical composition of silver NPs can be modified or they can even be completely oxidized in a reactive oxygen plasma. Figure 18 shows the optical properties of Ag NPs that passed through an argon plasma (solid curve) and an oxygen plasma (dashed curve). The shift in plasmon resonance indicates oxidation of Ag NPs because of oxygen plasma treatment. (One can speculate that, in the example shown in Figure 18, a very small core of the NP still remains metallic because the LSPR is still present in the UV region; however, stronger oxidation can be obtained by tuning of the plasma parameters.) Additional information provided by XPS analysis confirmed that Ag NPs are heavily oxidized after oxygen plasma treatment. First, results of silver ion release showed an enhanced rate of ion release from plasma oxidized Ag NPs during the first couple of hours, compared to similar metallic NPs. The observed effect of enhanced ion release could be beneficial for medical applications requiring, e.g. very fast and intensive treatments of wounds.

The combination of a GAS and a secondary plasma source like the HC, discussed above, is not restricted to "in-flight" plasma treatment of Ag NPs and opens prospects for synthesis of new nanostructures with unique properties. For instance, admixture of organic vapor into Ar HC plasma will promote plasma polymerization and, as a result, formation of core-shell NPs with a metallic core coated by a polymeric shell.

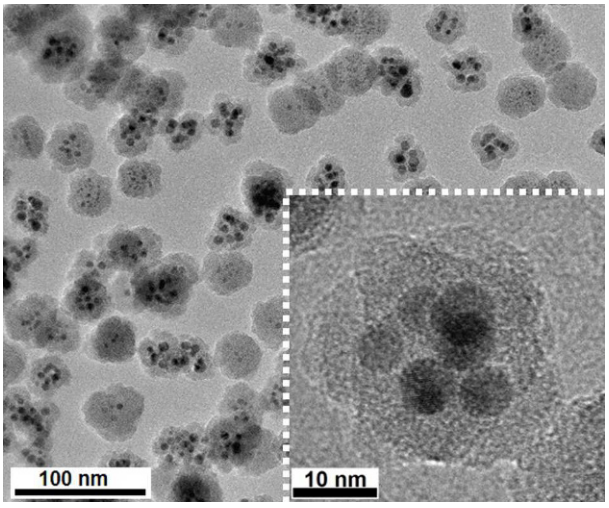

Fig. 19. TEM image of Ag/HMDSO multi core-shell NPs prepared by GAS source by controlled addition of HMDSO to the Ar gas during magnetron sputtering of Ag in a GAS. Deposition parameters: total working pressure 200 Pa, HMDSO concentration 0.45%, RF power 50 W.

A particularly striking example of the plasma-based formation of core-shell NPs is the fabrication of multiple core-shell particles shown in Figure 19. Here several Ag NPs were incorporated into a hexamethyldisiloxane (HMDSO) plasma polymer layer by controlled addition of HMDSO to the Ar gas during magnetron sputtering of Ag in a GAS. Details are reported elsewhere [76].

7 Conclusions

This paper gives an overview of the recent achievements in metal and metal oxide NP generation by a GAS based on magnetron sputtering. It was shown that GAS has the ability to synthesize of various types of NPs with desired properties. In particular, tailoring NP size and size distribution in a very broad range makes it attractive for deposition of nanocomposite thin films. Although a GAS is a very efficient tool for synthesis of noble metal NPs, reactive materials are very often problematic with respect to generation efficiency and reproducibility of deposition. Thus, a number of questions related to the reactive processes in GAS leading to NP formation, stability of their deposition and, in particular, huge efficiency of NP generation using pulsed sputtering have been clarified here. Moreover, fabrication of advanced nanomaterials with desired properties by using an external plasma source in combination with NP beam deposition (e.g. "in-flight" plasma treatment of NPs) was discussed.

Presented here are selected results gathered over the last few years within the framework of the collaborative research center (CRC) Transregio (TRR) 24 dealing with plasma-based growth and deposition of NPs and nanocomposite thin films by means of a GAS. The work was supported by the DFG through the projects B13 and A5 of the SFB TRR 24.

Author contribution statement

OP conducted the experiments or contributed to the experimental work and also wrote the manuscript. AMA conducted the experiments and analyzed the results related to the stability of Ti NP deposition and "in-flight" Ar plasma treatment of Ag NPs. TP conducted the experiments and analyzed the results related to Ag NP deposition by GAS (Figs. 5 and 6) and also contributed to the experiments on reactive processes in GAS (Fig. 9). KF, JWA, SW and MB performed KMC simulations and wrote the corresponding section. EV conducted the experiments and analyzed the results related to Si NP deposition. AH was involved in the experiments with Ti NP deposition and also performed TEM measurements. TS, HK and FF coordinated the work on plasma-based formation and deposition of NPs and also revised the final manuscript. All authors reviewed the final manuscript.

References

1. R. Jelinek, *Nanoparticles (De Gruyter Textbook)* (De Gruyter, Berlin, 2015)
2. F. Faupel, V. Zaporojtchenko, T. Strunskus, M. Elbahri, Adv. Eng. Mater. **12**, 1177 (2010)
3. A. Edelstein, R. Cammaratra, *Nanomaterials: synthesis, properties and applications* (Institute of Physics Publishing, Bristol, Philadelphia, 1998)
4. H. Kobayashi, A.T. Bell, M. Shen, Macromolecules **7**, 277 (1974)
5. K. Takahashi, K. Tachibana, J. Vac. Sci. Technol. A: Vac. Surf. Films **19**, 2055 (2001)
6. S.V. Vladimirov, K. Ostrikov, Plasmas Polym. **8**, 135 (2003)
7. I. Denysenko, J. Berndt, E. Kovačević, I. Stefanovic, V. Selenin, J. Winter, Phys. Plasmas **13**, 073507 (2006)
8. Y. Huttel, *Gas-phase synthesis of nanoparticles* (Wiley, Weinheim, 2017)
9. C.G. Granqvist, R.A. Buhrman, J. Appl. Phys. **47**, 2200 (1976)
10. K. Sattler, J. Mühlbach, E. Recknagel, Phys. Rev. Lett. **45**, 821 (1980)
11. F. Frank, W. Schulze, B. Tesche, J. Urban, B. Winter, Surf. Sci. **156**, 90 (1985)
12. H. Haberland, M. Karrais, M. Mall, Y. Thurner, J. Vac. Sci. Technol. A: Vac. Surf. Films **10**, 3266 (1992)
13. R. Lamber, A. Baalmann, N.I. Jaeger, G. Schulz-Ekloff, S. Wetjen, Adv. Mater. **6**, 223 (1994)
14. P. Milani, P. Piseri, E. Barborini, S. Iannotta, Mater. Sci. Forum **195**, 43 (1995)
15. M. Goto, J. Murakami, Y. Tai, K. Yoshimura, K. Igarashi, S. Tanemura, Z. Phys. D: Atoms Mol. Clust. **40**, 115 (1997)
16. D. Salz, R. Lamber, M. Wark, A. Baalmann, N. Jaeger, Phys. Chem. Chem. Phys. **1**, 4447 (1999)
17. C. Binns, Surf. Sci. Rep. **44**, 1 (2001)
18. S. Pratontep, S.J. Carroll, C. Xirouchaki, M. Streun, R.E. Palmer, Rev. Sci. Instrum. **76**, 045103 (2005)
19. A. Banerjee, R. Krishna, B. Das, Appl. Phys. A **90**, 299 (2007)
20. V.N. Popok, I. Barke, E.E. Campbell, K.H. Meiwes-Broer, Surf. Sci. Rep. **66**, 347 (2011)

21. V. Straák, S. Block, S. Drache, Z. Hubička, C.A. Helm, L. Jastrabík, M. Tichý, R. Hippler, Surf. Coat. Technol. **205**, 2755 (2011)
22. B. Gojdka, V. Zaporojtchenko, V. Hrkac, J. Xiong, L. Kienle, T. Strunskus, F. Faupel, Appl. Phys. Lett. **100**, 133104 (2012)
23. A.M. Zachary, I.L. Bolotin, L. Hanley, in *Nanofabrication using focused ion and electron beams: principles and applications*, edited by I. Utke, S. Moshkalev, P. Russell (Oxford University Press, New York, 2012), pp. 1–26
24. M. Ganeva, A. Pipa, R. Hippler, Surf. Coat. Technol. **213**, 41 (2012)
25. B. Briehl, H.M. Urbassek, J. Vac. Sci. Technol. A: Vac. Surf. Films **17**, 256 (1999)
26. B.M. Smirnov, Phys. Usp. **46**, 589 (2003)
27. E. Quesnel, E. Pauliac-Vaujour, V. Muffato, J. Appl. Phys. **107**, 054309 (2010)
28. P.V. Kashtanov, B.M. Smirnov, R. Hippler, Europhys. Lett. **91**, 63001 (2010)
29. A.A. Turkin, M.V. Dutka, Y.T. Pei, D.I. Vainshtein, J.T.M. De Hosson, J. Appl. Phys. **111**, 124326 (2012)
30. M. Hanif, R.R. Juluri, M. Chirumamilla, V.N. Popok, J. Polym. Sci. B: Polym. Phys. **54**, 1152 (2016)
31. J. Hanuš, T. Steinhartová, O. Kylián, J. Kousal, P. Malinský, A. Choukourov, A. Macková, H. Biederman, Plasma Process. Polym. **13**, 879 (2016)
32. H. Schaber, T. Martin, Surf. Sci. **156**, 64 (1985)
33. J. Kousal, O. Polonskyi, O. Kylián, A. Choukourov, A. Artemenko, J. Pešička, D. Slavínská, H. Biederman, Vacuum **96**, 32 (2013)
34. L. Zhang, J. Shao, X. Chen, Vacuum **129**, 105 (2016)
35. J.W. Abraham, A. Hinz, T. Strunskus, F. Faupel, M. Bonitz, Eur. Phys. J. D **72**, 92 (2018)
36. J.W. Abraham, T. Strunskus, F. Faupel, M. Bonitz, J. Appl. Phys. **119**, 185301 (2016)
37. K. Fujioka, Kinetic Monte Carlo Simulations of Cluster Growth in Magnetron Plasmas, PhD thesis, University of Kiel, 2015
38. A. Jansen, *An introduction to kinetic Monte Carlo simulations of surface reactions*, Lecture notes in physics (Springer-Verlag, Berlin, 2012)
39. L. Rosenthal, A. Filinov, M. Bonitz, V. Zaporojtchenko, F. Faupel, Contrib. Plasma Phys. **51**, 971 (2011)
40. M. Bonitz, L. Rosenthal, K. Fujioka, V. Zaporojtchenko, F. Faupel, H. Kersten, Contrib. Plasma Phys. **52**, 890 (2012)
41. L. Rosenthal, H. Greve, V. Zaporojtchenko, T. Strunskus, F. Faupel, M. Bonitz, J. Appl. Phys. **114**, 044305 (2013)
42. J.W. Abraham, N. Kongsuwan, T. Strunskus, F. Faupel, M. Bonitz, J. Appl. Phys. **117**, 014305 (2015)
43. M.G. Gauthier, G.W. Slater, Phys. Rev. E **70**, 015103 (2004)
44. B.M. Smirnov, Phys. Usp. **54**, 691 (2011)
45. M.V. Smoluchowski, Z. Phys. **17**, 557 (1916)
46. M. Ganeva, Formation of metal nano-size clusters with a DC magnetron-based gas aggregation source, PhD thesis, University of Greifswald, 2013
47. M. Ganeva, A.V. Pipa, B.M. Smirnov, P.V. Kashtanov, R. Hippler, Plasma Sources Sci. Technol. **22**, 045011 (2013)
48. K. Nanda, S. Sahu, S. Behera, Phys. Rev. A **66**, 84 (2002)
49. T. Peter, S. Rehders, U. Schürmann, T. Strunskus, V. Zaporojtchenko, F. Faupel, J. Nanopart. Res. **15**, 1710 (2013)
50. T. Acsente, R.F. Negrea, L.C. Nistor, C. Logofatu, E. Matei, R. Birjega, C. Grisolia, G. Dinescu, Eur. Phys. J. D **69**, 161 (2015)
51. G.E. Johnson, R. Colby, J. Laskin, Nanoscale **7**, 3491 (2015)
52. E. Palesch, A. Marek, P. Solar, O. Kylian, J. Vyskocil, H. Biederman, V. Cech, Thin Solid Films **544**, 593 (2013)
53. M. Ganeva, T. Peter, S. Bornholdt, H. Kersten, T. Strunskus, V. Zaporojtchenko, F. Faupel, R. Hippler, Contrib. Plasma Phys. **52**, 881 (2012)
54. S. Mondal, B. Satpati, S.R. Bhattacharyya, J. Nanosci. Nanotechnol. **15**, 611 (2015)
55. O. Kylián, J. Kratochvíl, J. Hanuš, O. Polonskyi, P. Solar, H. Biederman, Thin Solid Films **550**, 46 (2014)
56. O. Kylián, J. Prokeš, O. Polonskyi, J. Čechvala, J. Kousal, J. Pešička, J. Hanuš, H. Biederman, Thin Solid Films **571**, 13 (2014)
57. D.A. Eastham, B. Hamilton, P.M. Denby, Nanotechnology **13**, 51 (2002)
58. C. Xirouchaki, R.E. Palmer, Philos. Trans. Ser. A: Math. Phys. Eng. Sci. **362**, 117 (2004)
59. A.K. Srivastava, R. Yadev, V.N. Rai, T. Ganguly, S.K. Deb, Surface plasmon resonance in gold nanoparticles, in *AIP Conference Proceedings* (2012), Vol. 1447, pp. 305–306
60. B. Gojdka, V. Hrkac, J. Xiong, M. Gerken, L. Kienle, T. Strunskus, V. Zaporojtchenko, F. Faupel, J. Appl. Phys. **112**, 044303 (2012)
61. T. Peter, M. Wegner, V. Zaporojtchenko, T. Strunskus, S. Bornholdt, H. Kersten, F. Faupel, Surf. Coat. Technol. **205**, S38 (2011)
62. O. Polonskyi, O. Kylián, M. Drábik, J. Kousal, P. Solar, A. Artemenko, J. Čechvala, A. Choukourov, D. Slavínská, H. Biederman, J. Mater. Sci. **49**, 3352 (2014)
63. O. Polonskyi, P. Solar, O. Kylián, M. Drábik, A. Artemenko, J. Kousal, J. Hanuš, J. Pešička, I. Matolínová, E. Kolíbalová et al., Thin Solid Films **520**, 4155 (2012)
64. P. Solar, O. Kylián, O. Polonskyi, A. Artemenko, D. Arzhakov, M. Drábik, D. Slavínská, M. Vandrovcová, L. Bačáková, H. Biederman, Surf. Coat. Technol. **206**, 4335 (2012)
65. A. Marek, J. Valter, S. Kadlec, J. Vyskočil, Surf. Coat. Technol. **205**, S573 (2011)
66. T. Peter, O. Polonskyi, B. Gojdka, A. Mohammad Ahadi, T. Strunskus, V. Zaporojtchenko, H. Biederman, F. Faupel, J. Appl. Phys. **112**, 114321 (2012)
67. A.M. Ahadi, V. Zaporojtchenko, T. Peter, O. Polonskyi, T. Strunskus, F. Faupel, J. Nanopart. Res. **15**, 2125 (2013)
68. D. Depla, S. Mahieu, *Reactive sputter deposition* (Springer-Verlag, Berlin, 2008)
69. A.M. Ahadi, O. Polonskyi, U. Schürmann, T. Strunskus, F. Faupel, J. Phys. D: Appl. Phys. **48**, 035501 (2015)
70. O. Polonskyi, T. Peter, A. Mohammad Ahadi, A. Hinz, T. Strunskus, V. Zaporojtchenko, H. Biederman, F. Faupel, Appl. Phys. Lett. **103**, 033118 (2013)

71. W. Saddique, Nanoclusters Produced by High Power Impuls Magnetron Sputtering (HiPIMS), Master thesis, University of Kiel, 2015
72. M. Honda, Y. Kumamoto, A. Taguchi, Y. Saito, S. Kawata, Appl. Phys. Lett. **104**, 061108 (2014)
73. E. Vasiliauskaite, Nanoparticle Deposition by Pulsed Direct Current Magnetron Sputtering in a Reactive Gas Admixture, Master thesis, University of Kiel, 2014
74. A.M. Ahadi, T. Trottenberg, S. Rehders, T. Strunskus, H. Kersten, F. Faupel, Phys. Plasmas **22**, 083513 (2015)
75. A.M. Ahadi, A. Hinz, O. Polonskyi, T. Trottenberg, T. Strunskus, H. Kersten, F. Faupel, J. Vac. Sci. Technol. A: Vac. Surf. Films **34**, 021301 (2016)
76. P. Solar, O. Polonskyi, A. Olbricht, A. Hinz, A. Shelemin, O. Kylián, A. Choukourov, F. Faupel, H. Biederman, Sci. Rep. **7**, 8514 (2017)